A Photochromic Fluorescent Probe Strategy for the Super-resolution Imaging of Biologically Important Biomarkers

Xianzhi Chai,[a†] Hai-Hao Han,[a,b†] Adam C. Sedgwick,[d†] Na Li,[c] Yi Zang,[b] Tony D. James,[e] Junji Zhang,[a*] Xi-Le Hu,[a] Yang Yu,[c] Yao Li,[c] Yan Wang,[c] Jia Li[b*], Xiao-Peng He[a*] and He Tian[a]

[a]*Key Laboratory for Advanced Materials and Joint International Research Laboratory of Precision Chemistry and Molecular Engineering, Feringa Nobel Prize Scientist Joint Research Center, School of Chemistry and Molecular Engineering, Frontiers Center for Materiobiology and Dynamic Chemistry, East China University of Science and Technology, 130 Meilong Road, Shanghai 200237, People's Republic of China*

[b]*National Center for Drug Screening, State Key Laboratory of Drug Research, Shanghai Institute of Materia Medica, Chinese Academy of Sciences, 189 Guo Shoujing Rd., Shanghai 201203, P. R. China*

[c]*National Center for Protein Science Shanghai, Shanghai Institute of Biological Sciences, Chinese Academy of Sciences, Shanghai 200031, P. R. China*

[d]*Department of Chemistry, The University of Texas at Austin, 105 East 24th Street-A5300, Austin, Texas 78712-1224, USA.*

[e]*Department of Chemistry, University of Bath, Bath, BA2 7AY, UK.*

KEYWORDS. Fluorescence imaging, Photochromism, Human Serum Albumin (HSA), β-Galactosidase and STORM

ABSTRACT: Here, we report a β-galactosidase (β-Gal) responsive photochromic fluorescent probe **NpG** that was designed to pre-bind to human serum albumin (HSA) to form a probe/ protein hybrid **NpG@HSA**. The formation of **NpG@HSA** led to an increase in fluorescence emission (525 nm) corresponding to the binding of the fluorescent naphthalimide unit with HSA. In addition, this enabled visualization of the spiropyran fluorescence emission in aqueous media. Our probe/protein hybrid approach afforded a unique imaging platform with enhanced cell permeability and solubility that was capable of visualizing the cellular uptake of **NpG@HSA** before its activation by β-Gal. The β-Gal-mediated cleavage of the galactose unit within the **NpG@HSA** hybrid resulted in the formation of **NpM@HSA** and an increase in red fluorescence emission (620 nm). The resultant merocyanine unit was then able to undergo photoisomerization (merocyanine↔spiropyran) facilitating STORM (i.e. Stochastic Optical Reconstruction Microscopy) imaging with minimal phototoxicity and excellent photostability/reversibility. Using STORM, **NpG@HSA** was able to determine the subcellular distribution of β-Gal activity between cell lines with nanoscale precision. We believe this system represents a versatile imaging platform for the design of photochromic fluorescent probes suitable for illuminating the precise location of disease-specific biomarkers in various cellular processes.

INTRODUCTION

Enzymes are essential for the modification of a wide range of biologically important substrates.[1-2] This includes the post-translational modification of proteins and biomolecules that are directly involved in a number of key cellular events such as cell cycle, cell-cell interaction, signal transduction, and programmed cell death (apoptosis, proptosis and ferroptosis).[2-4] As a result, abnormal enzymatic activity has been linked to a range of diseases, which include inflammation, cancer and neurodegenerative disorders.[5-7] This dysregulation of an enzyme's activity can occur through a multitude of mechanisms, including simple changes to the physiological environment or by its subcellular distribution.[8] Therefore, identifying an enzyme's precise distribution and regulatory mechanisms within a specific cellular environment provides the foundation for identifying the relationship between its expression and a pathological process.[9-10] Despite the significant advancements made in the field of fluorescence sensing, the ability to determine the exact intracellular localization of an enzyme remains a challenging task, due to the diffraction limit of light and unsatisfactory spatial/temporal resolution of the currently reported fluorescent probes.[11-13]

The recent development of super-resolution-based technologies have revolutionized fluorescence-based imaging with the ability to visualize basic cellular structures with nanoscale precision by overcoming the diffraction limit of light.[14-18] Amongst the current super-resolution techniques, STORM (Stochastic Optical Reconstruction Microscopy) and PALM (photoactivated localization microscopy) rely on the use of fluorophores with switchable fluorescence emission profiles (photo-blinking).[15-17, 19-22] In these techniques, STORM/PALM facilitate the separation of spatially overlapping images of individual molecules to precisely determine their location. These techniques have enabled the super-resolution imaging of cellular architectures (e.g. tubulin)[23-25] and organelles such as mitochondria[26] and lysosomes.[27] More recently, STORM/PALM-based fluorescent probes have been reported for the detection of disease-related biomarkers.[28-29] These reported strategies rely on a dual-activatable approach (AND-logic) using a photoactivatable diazoindanone-based unit and enzyme cleavable motif, combined onto a single xanthene scaffold. Therefore, in the presence of a specific biomarker "AND" light, the probe is irreversibly photoactivated to afford a fluorescent product. The fluorescent product is then switched "off" by photobleaching before another subset is switched on. Repetition of this process allows for a super-resolution image to be constructed from a large number of individual molecular localizations. However, this photoinduced deprotection strategy combined with photobleaching could result in unwanted toxicity/phototoxicity issues, thus adversely affecting the

biological study in question.[30] Therefore, a reversible photoswitching system is highly desirable as it allows the same activated fluorophore to undergo multiple photoswitching cycles to obtain a super-resolution image with potentially less toxicity issues.

Spiropyran-based photochromic dyes (merocyanine↔spiropyran)[31] have been used as effective dyes for the super resolution imaging of cellular components[32] displaying excellent photoswitching properties, low photobleaching kinetics and minimal phototoxcitiy.[32-34] Such examples include the use of photoactuated unimolecular logical switching attained reconstruction (PULSAR) microscopy.[32] Unfortunately, the poor aqueous solubility of these photochromophores often results in their aggregation-caused quenching (ACQ), which has limited their biological application (Scheme 1a).[35] We are particularly interested in exploring the potential use of spiropyrans for biological applications, and as such we have previously developed functional spiropyran dyes containing ligands that allow the targeted imaging of disease specific cell lines with the additional ability to "double check" the dyes cellular uptake.[35, 36]

Inspired by these previous reports coupled with our interests in the development of fluorescent probes and super-resolution imaging technology,[37-40] we envisioned functionalizing the free phenol motif on the merocyanine fluorophore with an enzyme responsive unit would prevent photoisomerization and quench the fluorescence emission to afford an enzyme-based STORM fluorescent probe. In addition, we believed the incorporation of afluorescent naphthalimide unit would facilitate human serum albumin (HSA) binding and as a result provide appropriate aqueous solubility, cell permeability and allow the visualization of the cellular uptake of the STORM probe before its activation. Moreover, a clear fluorescence emission signal would be observed from the merocyanine unit upon activation(Scheme 1b).[35, 41, 42] In this study, we have chosen β-galactosidase (β-Gal) as a relevant example, however, it is important to note that the β-Gal reactive unit could be replaced with a reactive motif of choice to detect other biologically important biomarkers (i.e. H_2O_2, Esterases, proteases).

Here, a β-Gal-functionalized merocyanine fluorescent sensor **NpG** has been developed that was specifically designed to bind to human serum albumin (HSA) (Scheme 1a). In the presence of HSA, **NpG** formed a probe/ protein hybrid **NpG@HSA**, leading to an increase in fluorescence emission (525 nm), which corresponded to the binding of HSA with the fluorescent naphthalimide unit. This allowed the visualization of the cell uptake of **NpG@HSA**. Prior to activation, galactose-caged **NpG@HSA** was non-fluorescent at 620 nm and was unable to under-go photoisomerization. The β-Gal-mediated cleavage of the galactose unit resulted in the release of **NpM@HSA** with a concomitant increase in red fluorescence emission (620 nm). The release of the free phenol of **NpM@HSA** activated the system towards photoisomerization. The reversible photoisomerization and ON/OFF photo-blinking was then used for STORM imaging, which enabled the visualization of the subcellular localization of β-Gal in various cell lines with nanoscale precision (Scheme 1c).

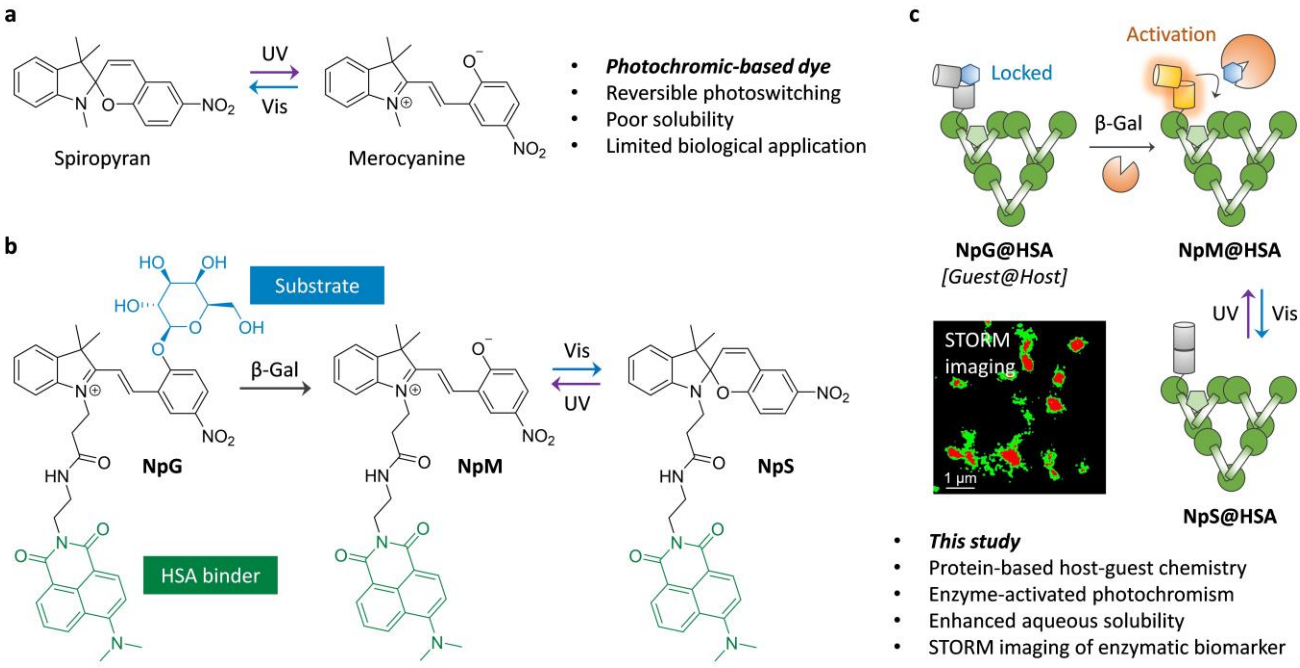

Scheme 1. (a) Photochromic spiropyran dye for reversible photoswitching applications.[31] (b) Structure and (c) fluorescence "turn-on" mechanism of **NpG@HSA** for the monitoring of β-Gal with the super-resolution imaging technique, STORM.

RESULTS AND DISCUSSION

In brief, **NpG** was synthesized by condensing a 2, 3, 3-trimethyl-3H-indole functionalized naphthalimide with 5-nitrosalicylaldehyde that was modified with an acetyl protected β-galactose group on the phenol unit. The subsequent deprotection of the acetate groups afforded **NpG** (Scheme S1). **NpS** was synthesized (Scheme S1) for use as a control in subsequent experiments. The protein hybridisation of **NpG** with HSA to form **NpG@HSA** was carried out as previously

reported and verified by fluorescence spectroscopy. The addition of HSA (0 – 50 μM) to a solution of **NpG** (5 μM) led to a remarkable increase in green fluorescence emssion (520 nm) corresponding to the formation of the probe/protein hybrid **NpG@HSA** (Figure S1a) (Figure S2).[43] This increase in fluorescence emission was indicative of the inclusion of **NpG** into the hydrophobic pocket of HSA owing to the enviromental sensitive nature of the fluorescent naphthalimide unit.[44] Job's plot analysis and competition-based experiments revealed a binding stoichiometry of 1:1 (Figure S1b) and a predominant inclusion into Site 1 (IIA domain) of HSA.[43] Isothermal titration calorimetry (ITC) and small angle X-ray scattering (SAXS) were carried out to further confirm these observations. As shown in Figure S1c and Figure S1d, a strong binding between **NpG** and HSA was observed with a binding affinity of K_d = 27.34 ± 1.93 μM. SAXS analysis demonstrated a substantial conformational change of the probe/protein hybrid at Site 1 (Figure S3). The fluorescence emission of **NpG@HSA** was shown to decrease when treated with a Site 1 binding drug (phenylbutazone), thus confirming our opinion that **NpG@HSA** was included in Site 1 of HSA (see ESI for SAXS data).[38, 41]

Next, we turned our attention towards the evaluation of **NpG@HSA** to selectively detect β-Gal in PBS buffer (10 mM, pH = 7.40). In the presence of β-Gal (10 U/mL), a decrease in UV-Vis absorption at 400 nm with a concomitant increase in the UV-Vis absorption at 530 nm was observed after 30 min (Figure 1a). This change in the UV-Vis absorption was accompanied with a significant increase in fluorescence emission intensity at 620 nm (Figure 1b and Figure S4a). High-performance liquid chromatography (HPLC) and high-resolution mass spectrometry (HRMS) (Figure S5) confirmed the changes in photophysical properties were the result of the β-Gal-mediated cleavage of **NpG@HSA** to **NpM@HSA**. Through fluorescence titrations, the limit of detection (LOD) was calculated as 6.1×10^{-4} U/mL (Figure 1c and Figure S4b). The steady-state kinetics of β-Gal towards **NpG@HSA** were determined using fluorescence spectroscopy, with the resultant fluorescence data analyzed using the Michaelis-Menten equation. A typical Michaelis-Menten curve was obtained (Figure S4c), which revealed a Michaelis-Menten constant of K_m = 4.34 μM and a V_{max} of 23.37 nM/s) (see SI for details). The selectivity of **NpG@HSA** towards other biological relevant species was then determined to demonstrate its applicability in bioimaging applications. As shown in Figure 1d, **NpG@HSA** exhibited high substrate selectivity for β-Gal over small-molecular metabolites and other glycosidases including β-glucosidase and β-glucoronidase.

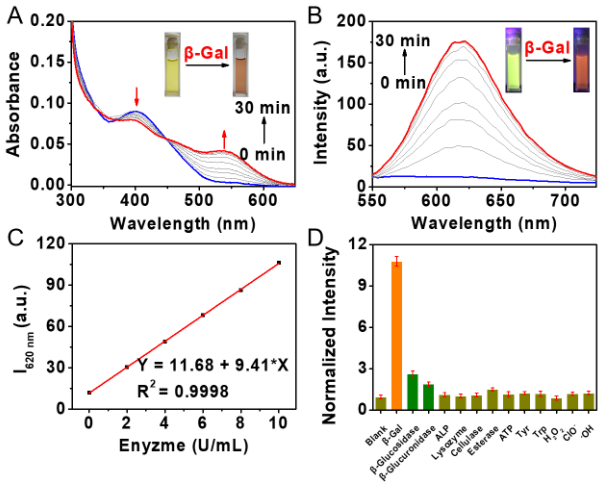

Figure 1 – The (a) time-dependent UV-Vis absorption and (b) fluorescence emission changes over time of **NpG@HSA** (5 μM) after incubation with β-Gal (10 U/mL) in PBS buffer (10 mM, pH = 7.4, 0.5% DMSO), respectively. Blue line: 0 min; Red line: 30 min. (c) Plots and linear fit of the fluorescence intensity of **NpM@HSA** at 620 nm as a function of β-Gal concentration (0-10 U/mL) after 30 min of incubation. (d) Fluorescence change at 620 nm of **NpG@HSA** with various biomolecules or enzymes after incubation for 30 min in PBS buffer (10 mM, pH = 7.4, 0.5% DMSO). H_2O_2 (0.1 mM), ClO^- (0.1 mM), $^{\cdot}OH$ (0.1 mM), ATP (0.1 mM), tyrosine (Tyr, 0.1 mM), tryptophan (Trp, 0.1 mM), β-glucosidase (10 U/mL), β-glucuronidase (10 U/mL), ALP (10 U/mL), lysozyme (10 U/mL), cellulase (10 U/mL), esterase (10 U/mL). All emissions were produced upon excitation at 530 nm.

Light-based experiments were then performed to determine the reversible photoisomerization ability of **NpM@HSA**. As shown in Figure 2a and Figure 2b, upon irradiation of **NpM@HSA** with visible light (550 nm, 150 mW cm^{-2}, 1 min), the fluorescence emission (620 nm) and UV-Vis absorption (530 nm) corresponding to **NpM@HSA** decreased sharply. HPLC analysis confirmed (Figure S5a), this was the photoisomerization of merocyanine (**NpM**) to the colorless, non-fluorescent spiropyran isomer (**NpS**). Subsequent UV irradiation (365 nm, 160 mW cm^{-2}, 5 min) of the same solution led to the regeneration of the photophysical properties unique to **NpM@HSA**, which corresponds to the photostationary state (PSS) of **NpS**. Several photoswitching cycles alternating visible (550 nm) and UV (365 nm) light irradiation (Figure 2c and Figure 2d) illustrated the excellent photostability of **NpM@HSA** and its applicability towards STORM-based imaging.

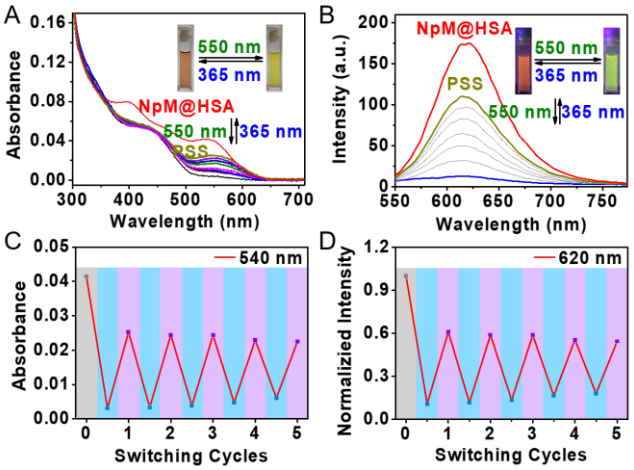

Figure 2 – The (a) UV-Vis absorption and (b) fluorescence emission changes of **NpM@HSA** upon irradiation with alternate visible light (550 nm, 150 mW cm^{-2}, 1 min) and UV light (365 nm, 160 mW cm^{-2}, 5 min), respectively. Red line: **NpM@HSA**; Blue line: Upon irradiation with 550 nm visible light for 1 min (mainly in the spiropyran isomer); Yellow line: Photostationary state (PSS) after irradiation of UV light for 5 min. (c) Photo-fatigue resistance performances of the UV-Vis absorption at 540 nm and (d) fluorescence emission at 620 nm of **NpM@HSA** upon irradiation with alternate visible light (550 nm, 150 mW cm^{-2}, 1 min) and UV light (365 nm, 160 mW cm^{-2}, 5 min), respectively. All emissions were produced upon excitation at 530 nm.

Cellular imaging experiments were carried out using the pre-formed probe/protein hybrid, **NpG@HSA** to examine its ability to image endogenous β-Gal. The treatment of human ovarian carcinoma cells (SKOV-3 cells), a cell line known to overexpress β-Gal with **NpG@HSA**,[45-47] led to fluorescence emissions corresponding to both naphthalimide (520 nm, green) and merocyanine (620 nm, red) being observed (Figure 3a). In contrast, pre-treatment of SKOV-3 cells with excess D-galactose – 1 mM (β-Gal inhibitor) prior to the addition of **NpG@HSA** resulted in only green fluorescence emission being observed. This was taken as evidence that the increase in red fluorescence emission in the absence of D-galactose is due to endogenous β-Gal (Figure 3a). Overall, these experiments demonstrate the excellent cell permeability of **NpG@HSA** and its ability to visualize endogenous β-Gal.

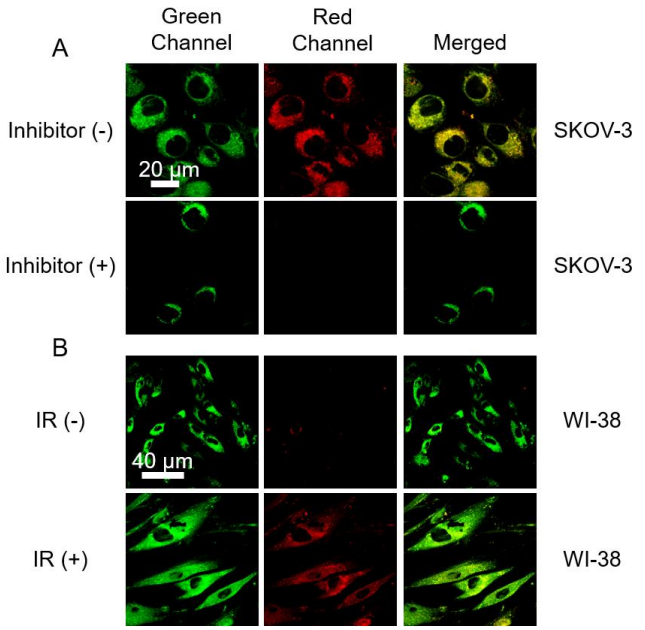

Figure 3 - β-Gal-activated fluorescence "OFF-ON" imaging in live cells of **NpG@HSA** (a) Confocal imaging of SKOV-3 cells incubated with **NpG@HSA** (20 μM) for 40 min with or without preincubated D-galactose (1 mM) as an inhibitor. (b) Confocal imaging of WI-38 cells incubated with **NpG@HSA** (20 μM) for 40 min with or without treatment by ionizing radiation (IR, 12 Gy). Green channel: Ex/Em = 488 / 530-540 nm; Red channel: Ex/Em = 559 / 600-620 nm.

With these results in hand, the ability of **NpG@HSA** to differentiate between the β-Gal activity of ovarian cancer and normal cell lines was then evaluated. The three different cell lines, OVCAR-3, SKOV-3 and HUVEC were chosen and treated with **NpG@HSA**. As shown in Figure S6, each cell line displayed significant green fluorescence emission further demonstrating the excellent cell permeability of **NpG@HSA** and utility of the probe/protein hybrid to visualize cellular uptake. As expected, a clear red fluorescence emission was observed in both ovarian cancer cells OVCAR-3 and SKOV-3, whereas HUVEC, a human umbilical vein endothelium cell line displayed only green fluorescence emission. This result further demonstrates the unique ability of the imaging platform to simultaneously visualize cellular uptake and monitor enzymatic activity within various cell lines thus removing any potential false negatives.

To demonstrate the full potential of **NpG@HSA** for monitioring intracellular β-Gal, we then evaluated its ability to visualise changes in β-Gal levels during cell senescence. In these experiments, WI-38 cells (human embryonic lung diploid fibroblasts) were incubated with **NpG@HSA**. Similar to previous experiments, WI-38 cells displayed initial green fluorescence emission (Figure 3b, green channel). Then, as predicted, no red fluorescence emission was observed (Figure 3b, red channel), due to low endogeous levels of β-Gal being present in WI-38 cells. However, treatment of WI-38 cells with ionizing radiation (IR, 12 Gy, 24 h)) induced cell senescence,[48-50] and led to a significant enhancement in red fluorescence emission, which was indicative of an increase in β-Gal levels (Figure 3b,). A commercial β-Gal biochemical assay was used to confirm the increase in red fluorescence emission in WI-38 cells exposed to ionising irradiation was the result of an increase in β-Gal expression (Figure S7). Again, these results are in

agreement with previous reports that β-Gal is overexpressed in senescent cells.[51] Note - hydrogen peroxide (H_2O_2) (150 μM, 2 h) was shown as an alternative strategy to induce cell senescence and increase β-Gal expression (Figure S7).[50] H_2O_2 was used as an additional cell senescence inducing strategy due to the shorter time periods required to induce cell senescence in comparison to the ionising irradiation protocol (H_2O_2 – 12/ 48 h vs IR – 12 days).

Subsequently, visible/UV light irradiation of both SKOV-3 and senescent cells was carried out, and a reversible "ON/OFF" change in the fluorescence signal was observed (Figure 4a, and Figure 4c). Remarkably, the "photo-blinking" effect was repeated over several cycles with no obvious change in fluorescence intensity (Figure 4b and Figure 4d). Both D-galactose pre-treated SKOV-3 cells and non-irradiated WI-38 cells produce no red fluorescence emission nor photo-blinking, irrespective of either UV or visible irradiation (Figure 4a, and Figure 4c). In addition, **NpG@HSA** displayed almost no cytotoxicity (Figure S8a) including no phototoxicity for the photo-switching experiments (UV light: 365 nm, 160 mW cm^{-2}, 5 min per cycle and visible light: 550 nm, 150 mW cm^{-2}, 10 min per cycle; Figure S8b).

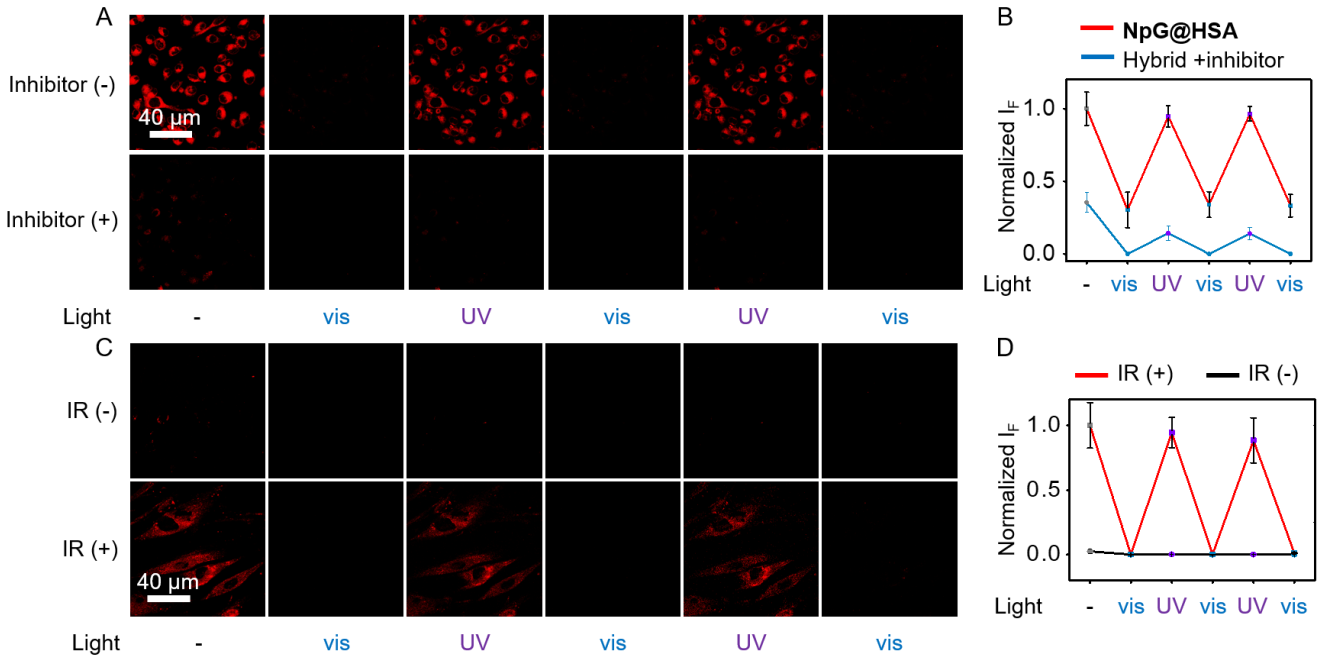

Figure 4 - (a) Fluorescence imaging of SKOV-3 cells incubated with **NpG@HSA** (20 μM) for 40 min in the absence (line 1) and presence of D-galactose (1 mM, line 2) upon alternate irradiation with UV and visible light. (b) Fluorescence quantification of the images shown in Fig. 4a with photoswitching cycles. (c) Fluorescence imaging of endogenous β-Gal in WI-38 cells with or without ionizing irradiation after incubation with **NpG@HSA** (20 μM) for 40 min. (d) Fluorescence quantification of the images shown in Fig. 4d with photoswitching cycles. Green channel: Ex/Em = 488 / 530-540 nm; Red channel: Ex/Em = 559 / 600-620 nm. For photoswitching excitation: UV, 405 nm, 30 s; Vis, 559 nm, 10 min.

Encouraged by the above results, we then applied our enzyme-activated **NpG@HSA** photochromic probe for the STORM-based imaging of endogenous β-Gal distributions in both ovarian cancer and aging cells. STORM images were recorded on an electron multiplying charge-coupled device (EMCCD) camera running at 52-53 ms per frame. After optimization of the protocol,[18] it was possible to acquire images with enough switching events to render meaningful STORM images, the number of frames collected was up to 16000 (Figure 5, Figure S9 and Video S1). To extract dynamic information from these images, the 16000 frames obtained were divided and reconstructed to examine the gradual increase in the activated fluorescent "hotspot". The images were separated and reconstructed from 0 - 4000 frames (Figure S9a and Figure S9c), 0 - 8000 frames (Figure S9b and Figure S9d) and 0 - 16000 frames (Figure 5b and Figure 5f). The red areas shown in Figure 5 and Figure S9, which are known as clusters indicate when the fluorescence intensity is higher than a set threshold fluorescence intensity (two-fold), whereas the green areas/dots represent an intensity below the threshold (green objects). Interestingly, red clusters were shown to become densely populated in senescent WI-38 cells with a specific distribution as the frame number increased, suggesting the β-Gal in senescent cells is localized (Figure 5b, Figure S9a and Figure S9b). On the contrary, in SKOV-3 cells, probe-concentrated red clusters were hardly observed with green objects predominating, suggesting a random distribution of β-Gal in the cytoplasm (Figure 5f, Figure S9c and Figure S9d). Co-localization experiments using LysoTracker produced a high Pearson's correlation coefficient (0.955) suggesting the localization in senescent cells was at the lysosome. This is supported by previous reports.[45-47, 51-52] A poor Pearson's correlation efficient (0.496) was observed for SKOV-3 cells, which further confirmed the random distribution throughout the cytoplasm (Figure S10). Remarkably, these STORM images displayed a high resolution with an average full-width-at-half maximum (FWHM) diameter of 80 nm in WI-38 cells (Figure 5c, top and Figure 5d, blue line) and 74 nm in SKOV-3 cells (Figure 5g, top and Figure 5h, blue line), which are significantly greater when compared with traditional confocal fluorescence images (for WI-38 cells, 1 μm, Figure 5c, bottom and Figure 5d, red line; for SKOV-3 cells, 4 μm, Figure 5g, bottom and Figure 5h, red line). These results demonstrate

the utility of STORM to provide more detailed information on the precise distribution of intracellular β-Gal with greater resolution and potentially overcoming the limitations of current fluorescent probes.

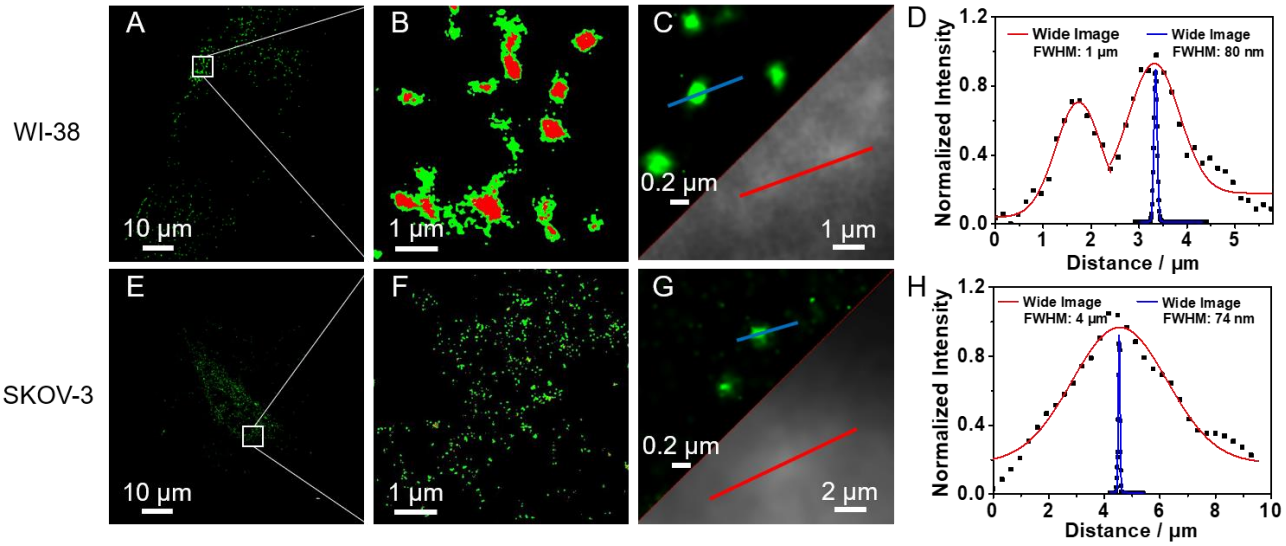

Figure 5 – Subcellular imaging of β-galactosidase in cancerous and senescent cells using STORM. (a) Super-resolution images (STORM) of senescent WI-38 cells and (e) SKOV-3 cells incubated with **NpG@HSA** (20 μM), respectively. (b) Zoomed images of Fig. 5a reconstructed from 16000 frames. Scale bar: 1 μm. (f) Zoomed images of Fig. 5d reconstructed from 16000 frames. Scale bar: 1 μm. (c-d) The calculation of FWHM in WI-38 cells of STORM image and wide image, respectively. (g-h) The calculation of FWHM in SKOV-3 cells of STORM image and wide image, respectively.

To validate our results from above, voxels were extracted from the fluorescence signals and processed to illustrate the formation of clusters using the algorithm of Cell Membrane Detection using the Bitplane Imaris software (Figure S11).[53] The center of each fluorescent signal were labeled as spots and each voxel was mapped with an intensity representing the distance to the adjacent spot. As shown in Figure S11a and Figure S11d, the voxels were divided into different color polygons according to the distribution of distance. A gradient color change could be observed for the image of senescent WI-38 cells, indicating a possible existence of clusters. For the image of SKOV-3 cells, a randomly distributed emission was observed. Zoomed images were reconstructed from 0-8000 frames (Figure S11b and Figure S11e) and from 0-16000 frames (Figure S11c and Figure S11f). The red clusters of polygons in the images of senescent WI-38 cells increased remarkably as the frame number increases, while the green objects in images of SKOV-3 cells remained dominant regardless of the frame numbers. The results from these two methods clearly indicate that **NpG@HSA** can be used for the mapping of intracellular β-Gal activity with high precision using STORM imaging. Overall, the results indicate that our design strategy has produced a new versatile imaging platform that could be used to develop a range of fluorescent probes suitable for STORM-based imaging.

CONCLUSIONS

In summary, we have developed an enzyme-responsive photochromic fluorescent probe/ HSA assemble (**NpG@HSA**) that was able to image β-Gal in ovarian cancer and senescent cells. **NpG@HSA** provides enhanced cell permeability and solubility facilitating the visualization of cellular uptake. The β-Gal-mediated deprotection of the galactose unit on **NpG@HSA** released the photo-active merocyanine. STORM-based imaging of β-Gal in different cell lines was then possible due to the excellent photo-switching properties of the merocyanine unit. Using STORM imaging, the cellular distribution of β-Gal was visualized at an unprecedented nanoscale level. These results provide more detailed information on the precise distribution of lysosomal β-Gal in senescent cells and the random distribution in ovarian cancer cells. We anticipate that our enzyme responsive, photochromic/ protein fluorescent probe strategy will inspire others to develop a range of fluorescent probes suitable for the super-resolution imaging of disease-related biomarkers.

METHODS

Ionizing radiation (IR) induced cell senescence procedures. WI-38 cells (human embryonic lung diploid fibroblasts) were cultured in 5 % CO_2 atmosphere under 37°C in Eagle's Minimum Essential Medium (Sigma, USA) supplemented with 10% fetal bovine serum (Gibco, Gland Island, NY, USA). In all experiments, cells at early passages (< 10 passages) were used and each of the passage reached approximately 90 % confluence. Exponentially-growing WI-38 cells at passage 6 were plated into 6 cm cell culture dish (Corning, USA) and after 24 h, these cell culture dishes were irradiated with doses of 12 Gy at room temperature to induce cell senescence. After irradiation, WI-38 cells were senescent by day 12 with 90% or more cells positive for senescence associated β-galactosidase activity.

Oxidative stress-induced cell senescence by treatment with exogenous H_2O_2. Exponentially-growing WI-38 cells at passage 6 were plated into 6 cm cell culture dish (Corning, USA) and treated with H_2O_2 (150 μM, Sinopharm Chemical Reagent Co.,Ltd, Shanghai, China) for 2h, followed by 12 h or 48 h continuous culture.

Cytochemical staining method. Experiments were performed using a senescence β-galactosidase staining kit according to the manufacturer's instructions (Beyotime, Shanghai, China). Cells

were plated on 96-well plates in growth medium. After 24 h, the cells were washed with PBS and fixed for 15 min. After dilution with PBS, the cells were washed again with PBS and stained with X-Gal solution for 24 h at 37 ºC. Finally, bright field images were collected on an Olympus IX71 microscope.

Confocal laser scanning microscopy for imaging of endogenous β-Gal. Cells cultured in growth medium supplemented with 10% FBS were added to a 24-well microplate. Cells were maintained in a humidified atmosphere of 5% CO_2 and 95% air at 37 °C overnight, and then incubated with **NpG@HSA** (20 μM) for 40 min. Then the cells on the microplate were rinsed using warm PBS and fixed by 4 % paraformaldehyde for 20 min at room temperature. Immediately after sealing, the fluorescence was detected and photographed with confocal laser scanning microscopy (Olympus, Japan, green channel excitation: 488 nm, emission: 530-540 nm; red channel excitation: 559 nm, emission: 600-620 nm). After imaging of endogenous β-galactosidase with confocal laser scanning microscopy (Olympus, Japan, green channel excitation: 488 nm, emission: 530-540 nm; red channel excitation: 559 nm, emission: 600-620 nm), the slide was irradiated with visible light (559 nm laser) in a darkroom for 10 min, and then the two channels of fluorescence were detected and photographed with the microscope. To test the duplexed fluorescence switching, the slide was further irradiated with UV light (405 nm laser) in the darkroom for 30 s, and then the two channels of fluorescence were detected and photographed with the microscope. The UV/Vis irradiation was repeatedly carried out for at least three cycles.

Cell viability and phototoxicity assay. SKOV3 cells (ATCC® HTB-77™) were plated on 96-well plates in growth medium (McCoy's 5A; Gibco, Gland Island, NY, USA) for 24 h and then treated with different concentrations of **NpG@HSA**. After 48 h incubation, MTS/PMS solution was added. After 2 h incubation, the absorbance was measured at 490 nm using a M5 microplate reader (Molecular Device, USA). The optical density from the MTS assay was directly proportional to the number of viable cells. For the phototoxicity assay, UV light (365 nm, 160 mW cm^{-2}, 5 min) and visible light (550 nm, 150 mW cm^{-2}, 10 min) was used to irradiate alternately for different cycles. Then the cells were incubated in dark at 37 ºC for 48 h and the viability was measured through the MTS cell proliferation assay.

Co-localization experiment. Cells cultured in growth medium supplemented with 10% FBS were added to a 24-well microplate. Cells were maintained in a humidified atmosphere of 5% CO_2 and 95% air at 37 °C overnight and were treated using H_2O_2-induced cell senescence assay. Then, cells were incubated sequentially with **NpG@HSA** (20 μM) and LysoTracker® Deep Red (500 nM, Thermo Fisher Scientific) for 40 min. Then the cells on the microplate were rinsed by warm PBS and fixed by 4% paraformaldehyde for 20 min at room temperature. Immediately after sealing, the fluorescence was detected and photographed with confocal laser scanning microscopy (Leica TCS SP8, Leica Microsystems, Wetzlar, Germany, red channel excitation: 559 nm, emission: 600-620 nm; Lyso tracker channel excitation: 633nm, emission: 650-670 nm).

STORM imaging protocol. Super-resolution STORM imaging was performed on a custom modified Nikon N-STORM microscope[54] equipped with a motorized inverted microscope ECLIPSE Ti-E, an Apochromat TIRF 100 × oil immersion lens with a numerical aperture of 1.49 (Nikon), an electron multiplying charge-coupled device (EMCCD) camera (iXon3 DU-897E, Andor Technology), a quad band filter composed of a quad line beam splitter (zt405/488/561/640rpc TIRF, Chroma Technology Corporation) and a quad line emission filter (brightline HC 446, 523, 600, 677, Semrock, Inc.). The TIRF angle was adjusted to oblique incidence excitation at the value of 3920-3950, allowing the capture of images at about 1 μm depth of samples. The focus was kept stable during acquisition using Nikon focus system. Before the STORM imaging experiments, we first confirmed the feasibility of merocyanine imaging using total internal reflection (TIRF) excitation at 561 nm and detection with a 630/60 nm bandpass filter. Furthermore, the photoactivation was proved to be efficient under 405 nm laser irradiation to modulate the photochromic processes. During the imaging experiments, the fluorescent state (merocyanine isomer) was converted to the dark state (spiro isomer) under 561 nm visible light . Then, the 405 nm diode laser (CUBE 405-100C, Coherent Inc.) was used for switching back the fluorophores from dark to the fluorescent state, meanwhile the 561 nm continuous wave visible fibre laser was used to excite the merocyanine isomer for collecting the cell images. The integration time of the EMCCD camera was 52-53 ms per frame. To image intracellular β-galactosidase, cells were seeded on a glass dish, and when the density was appropriate, cells were stained with **NpG@HSA** for 40 min and cells were fixed with 4% PFA, followed by three washes with PBS buffer. Before imaging, the buffer in the dish was replaced with the imaging buffer containing 7 μL GLOX solution and 500 μL Buffer B (50 mM, Tris-HCl, pH = 8.0 and 10 % Glucose).

Analysis of STORM imaging data. Super-resolution images were reconstructed from 0-4000 (71s in SKOV-3 and 162 s in WI-38 senescent cells), 0-8000 (142s in SKOV-3 and 324 s in WI-38 senescent cells) and 16000 frames (285s in SKOV-3 and 651 s in WI-38 senescent cells) using the N-STORM analysis module of NIS Elements AR (Laboratory imaging s.r.o.) and then the fluorescence signal of images was processed with the Image J software. Clusters were defined as regions where the fluorescence intensity is larger than twice the average intensity of the whole image and marked red. Objects were defined as regions where the fluorescence intensity is lower than twice the average intensity of the whole image and marked green. For the single-voxel localization analysis, voxels of molecular fluorescence signal were localized using the Bitplane Imaris software. The centers of signals were labelled as spots and the XTensions plug-in of distance transformation computes and creates a new channel. The created channel intensity values are based on the distance to a spot. Each voxel was mapped with an intensity representing the minimum distance measured to the nearest spot's center. A higher intensity value corresponds to a larger distance to a spot. The center of the spot defines the origin of the distance transformation. Voxels in the center of the spot are always set to have an intensity value of 0. The localization of voxels was divided into different polygons areas according to the distribution of distance by the algorithm of Cell Membrane Detection in Imaris. The Polygon area size represents the fluorescence density distribution. Objects were defined as regions that enclose polygons in which the area (represents the fluorescence density distribution) value is lower than half of the average area value of the whole image. Clusters were defined as regions in which the area value is lower than quarter of the area intensity value of the whole image.

ASSOCIATED CONTENT

Supporting Information

Detailed synthesis, characterization and photophysical data; ^{1}H spectra, IR spectra, MS spectra. These materials are available free of charge *via* the Internet at http://pubs.acs.org.

AUTHOR INFORMATION

Corresponding Author

*Junji Zhang. Email: zhangjunji@ecust.edu.cn
*Jia Li. Email: jli@simm.ac.cn
*Xiao-Peng He. Email: xphe@ecust.edu.cn

Author Contributions

† These authors contributed equally to this work.

Notes

The authors declare no competing financial interest.

ACKNOWLEDGMENT

This work was supported by the NSFC (21788102, 91853201, 21878086 and 21722801), Shanghai Municipal Science and Technology Major Project (2018SHZDZX03), The National Key Sci-Tech Special Projects of Infection Diseases of China (2018ZX10732202), the international cooperation program of Shanghai Science and Technology Committee (17520750100) and the Shanghai Rising-Star Program (19QA1402500 to J. Z.). The authors wish to acknowledge Jie Gao and Ying Dong for help in cell culture. TDJ wishes to thank the Royal Society for a Wolfson Research Merit Award.

REFERENCES

1. Cuesta, S. M.; Rahman, S. A.; Furnham, N.; Thornton, J. M., The Classification and Evolution of Enzyme Function. *Biophys. J.* **2015**, *109* (6), 1082-1086.
2. Walsh, C. T.; Garneau-Tsodikova, S.; Gatto, G. J., Protein posttranslational modifications: The chemistry of proteome diversifications. *Angew. Chem.-Intl. Ed.* **2005**, *44* (45), 7342-7372.
3. Reinders, J.; Sickmann, A., Modificomics: Posttranslational modifications beyond protein phosphorylation and glycosylation. *Biomol. Eng* **2007**, *24* (2), 169-177.
4. Li, J.; Yuan, J., Caspases in apoptosis and beyond. *Oncogene.* **2008**, *27* (48), 6194-6206.
5. Bond, M. R.; Hanover, J. A., O-GlcNAc Cycling: A Link Between Metabolism and Chronic Disease. In *Annual Review of Nutrition*, Cousins, R. J., Ed. **2013**, *33*, 205-229.
6. Pandey, K. C.; De, S.; Mishra, P. K., Role of Proteases in Chronic Obstructive Pulmonary Disease. *Front. Pharmacol.* **2017**, *8*, 512.
7. Gupta, R.; Ambasta, R. K.; Kumar, P., Pharmacological intervention of histone deacetylase enzymes in the neurodegenerative disorders. *Life Sci.* **2020**, *243*, 117278.
8. Robinson, P. K., Enzymes: principles and biotechnological applications. In *Understanding Biochemistry: Enzymes and Membranes*, **2015**, *59*, 1-41.
9. Zhou, L.; Zhu, D. Y., Neuronal nitric oxide synthase: Structure, subcellular localization, regulation, and clinical implications. *Nitric Oxide-Biol. CH.* **2009**, *20* (4), 223-230.
10. Wanders, R. J. A.; Waterham, H. R.; Ferdinandusse, S., Metabolic Interplay between Peroxisomes and Other Subcellular Organelles Including Mitochondria and the Endoplasmic Reticulum. *Front. Cell Dev. Biol.* **2016**, *3*, UNSP 83.
11. Zhang, J. J.; Chai, X. Z.; He, X. P.; Kim, H. J.; Yoon, J.; Tian, H., Fluorogenic probes for disease-relevant enzymes. *Chem. Soc. Rev.* **2019**, *48* (2), 683-722.
12. Wu, D.; Sedgwick, A. C.; Gunnlaugsson, T.; Akkaya, E. U.; Yoon, J.; James, T. D., Fluorescent chemosensors: the past, present and future. *Chem. Soc. Rev.* **2017**, *46* (23), 7105-7123.
13. Sedgwick, A. C.; Wu, L. L.; Han, H. H.; Bull, S. D.; He, X. P.; James, T. D.; Sessler, J. L.; Tang, B. Z.; Tian, H.; Yoon, J., Excited-state intramolecular proton-transfer (ESIPT) based fluorescence sensors and imaging agents. *Chem. Soc. Rev.* **2018**, *47* (23), 8842-8880.
14. Grotjohann, T.; Testa, I.; Leutenegger, M.; Bock, H.; Urban, N. T.; Lavoie-Cardinal, F.; Willig, K. I.; Eggeling, C.; Jakobs, S.; Hell, S. W., Diffraction-unlimited all-optical imaging and writing with a photochromic GFP. *Nature.* **2011**, *478* (7368), 204-208.
15. Chozinski, T. J.; Gagnon, L. A.; Vaughan, J. C. Twinkle, twinkle little star: Photoswitchable fluorophores for super-resolution imaging. FEBS Letters. **2014**, 588, 3603-3612
16. Shim, S. H.; Xia, C. L.; Zhong, G. S.; Babcock, H. P.; Vaughan, J. C.; Huang, B.; Wang, X.; Xu, C.; Bi, G. Q.; Zhuang, X. W., Super-resolution fluorescence imaging of organelles in live cells with photoswitchable membrane probes. *Proc. Natl. Acad. Sci. U. S. A.* **2012**, *109* (35), 13978-13983.
17. Sengupta, P.; van Engelenburg, S. B.; Lippincott-Schwartz, J., Superresolution Imaging of Biological Systems Using Photoactivated Localization Microscopy. *Chem. Rev.* **2014**, *114* (6), 3189-3202.
18. Rust, M. J.; Bates, M.; Zhuang, X. W., Sub-diffraction-limit imaging by stochastic optical reconstruction microscopy (STORM). *Nat. Methods* **2006,** *3* (10), 793-795.
19. Samanta, S.; Gong, W. J.; Li, W.; Sharma, A.; Shim, I.; Zhang, W.; Das, P.; Pan, W. H.; Liu, L. W.; Yang, Z. G.; Qu, J. L.; Kim, J. S., Organic fluorescent probes for stochastic optical reconstruction microscopy (STORM): Recent highlights. *Coord. Chem. Rev.* **2019,** *380*, 17-34.
20. Li, H. L.; Vaughan, J. C., Switchable Fluorophores for Single-Molecule Localization Microscopy. *Chem. Rev.* **2018**, *118* (18), 9412-9454.
21. Dempsey, G. T.; Vaughan, J. C.; Chen, K. H.; Bates, M.; Zhuang, X. W., Evaluation of fluorophores for optimal performance in localization-based super-resolution imaging. *Nat. Methods.* **2011**, *8* (12), 1027-1036.
22. Deniz, E.; Tomasulo, M.; Cusido, J.; Yildiz, I.; Petriella, M.; Bossi, M. L.; Sortino, S.; Raymo, F. M., Photoactivatable Fluorophores for Super-Resolution Imaging Based on Oxazine Auxochromes. *J. Phys. Chem. C.* **2012**, *116* (10), 6058-6068.
23. Roubinet, B.; Weber, M.; Shojaei, H.; Bates, M.; Bossi, M. L.; Beloy, V. N.; Irie, M.; Hell, S. W., Fluorescent Photoswitchable Diarylethenes for Biolabeling and Single-Molecule Localization Microscopies with Optical Superresolution. *J. Am. Chem. Soc.* **2017**, *139* (19), 6611-6620.
24. Uno, S. N.; Kamiya, M.; Yoshihara, T.; Sugawara, K.; Okabe, K.; Tarhan, M. C.; Fujita, H.; Funatsu, T.; Okada, Y.; Tobita, S.; Urano, Y., A spontaneously blinking fluorophore based on intramolecular spirocyclization for live-cell super-resolution imaging. *Nat. Chem.* **2014**, *6* (8), 681-689.
25. Uno, S.; Kamiya, M.; Morozumi, A.; Urano, Y., A green-light-emitting, spontaneously blinking fluorophore based on intramolecular spirocyclization for dual-colour super-resolution imaging. *Chem. Commun.* **2018**, *54* (1), 102-105.
26. Ye, Z. W.; Yu, H. B.; Yang, W.; Zheng, Y.; Li, N.; Bian, H.; Wang, Z. C.; Liu, Q.; Song, Y. T.; Zhang, M. Y.; Xiao, Y., Strategy to Lengthen the On-Time of Photochromic Rhodamine Spirolactam for Super-resolution Photoactivated Localization Microscopy. *J. Am. Chem. Soc.* **2019**, *141* (16), 6527-6536.
27. Halabi, E. A.; Pinotsi, D.; Rivera-Fuentes, P., Photoregulated fluxional fluorophores for live-cell super-resolution microscopy with no apparent photobleaching. *Nat. Commun.* **2019**, *10*, 1232.
28. Thiel, Z.; Rivera-Fuentes, P., Single-Molecule Imaging of Active Mitochondrial Nitroreductases Using a Photo-Crosslinking Fluorescent Sensor. *Angew. Chem.-Intl. Ed.* **2019**, *58* (33), 11474-11478.
29. Halabi, E. A.; Thiel, Z.; Trapp, N.; Pinotsi, D.; Rivera-Fuentes, P., A Photoactivatable Probe for Super-Resolution Imaging of Enzymatic Activity in Live Cells. *J. Am. Chem. Soc.* **2017**, *139* (37), 13200-13207.

30. Waldchen, S.; Lehmann, J.; Klein, T.; van de Linde, S.; Sauer, M., Light-induced cell damage in live-cell super-resolution microscopy. *Sci. Rep.* **2015**, *5*, 15348.
31. Klajn, R., Spiropyran-based dynamic materials. *Chem. Soc. Rev.* **2014**, *43* (1), 148-184.
32. Hu, D. H.; Tian, Z. Y.; Wu, W. W.; Wan, W.; Li, A. D. Q., Photoswitchable Nanoparticles Enable High-Resolution Cell Imaging: PULSAR Microscopy. *J. Am. Chem. Soc.* **2008**, *130* (46), 15279-15281.
33. Zhu, M. Q.; Zhang, G. F.; Hu, Z.; Aldred, M. P.; Li, C.; Gong, W. L.; Chen, T.; Huang, Z. L.; Liu, S. Y., Reversible Fluorescence Switching of Spiropyran-Conjugated Biodegradable Nanoparticles for Super-Resolution Fluorescence Imaging. *Macromolecules* **2014**, *47* (5), 1543-1552.
34. Zhang, H., Wang, C., Jiang, T., Guo, H., Wang, G., Cai, X., Yang, L., Zhang, Y., Yu, H., Wang, H., Jiang, K., Microtubule-Targetable Fluorescent Probe: Site-Specific Detection and Super-Resolution Imaging of Ultratrace Tubulin in Microtubules of Living Cancer Cells. Anal. Chem. **2015**, 87, 10, 5216–5222
35. Fu, Y. X.; Han, H. H.; Zhang, J. J.; He, X. P.; Feringa, B. L.; Tian, H., Photocontrolled Fluorescence "Double-Check" Bioimaging Enabled by a Glycoprobe-Protein Hybrid. *J. Am. Chem. Soc.* **2018**, *140* (28), 8671-8674.
36. Zhang, J. J.; Fu, Y. X.; Han, H. H.; Zang, Y.; Li, J.; He, X. P.; Feringa, B. L.; Tian, H., Remote light-controlled intracellular target recognition by photochromic fluorescent glycoprobes. *Nat. Commun.* **2017**, *8*, 987.
37. Xu, K.; Shim, S. H.; Zhuang, X. W., Super-Resolution Imaging Through Stochastic Switching and Localization of Single Molecules: An Overview. In *Far-Field Optical Nanoscopy*, Tinnefeld, P.; Eggeling, C.; Hell, S. W., Eds. **2015**, *14*, 27-64.
38. Han, H. H.; Sedgwick, A. C.; Shang, Y.; Li, N.; Liu, T. T.; Li, B. H.; Yu, K. Q.; Zang, Y.; Brewster, J. T.; Odyniec, M. L.; Weber, M.; Bull, S. D.; Li, J.; Sessler, J. L.; James, T. D.; He, X. P.; Tian, H., Protein encapsulation: a new approach for improving the capability of small-molecule fluorogenic probes. *Chem. Sci.* **2020**, *11* (4), 1107-1113.
39. Sedgwick, A. C.; Han, H. H.; Gardiner, J. E.; Bull, S. D.; He, X. P.; James, T. D., The development of a novel AND logic based fluorescence probe for the detection of peroxynitrite and GSH. *Chem. Sci.* **2018**, *9* (15), 3672-3676.
40. Odyniec, M. L.; Sedgwick, A. C.; Swan, A. H.; Weber, M.; Tang, T. M. S.; Gardiner, J. E.; Zhang, M.; Jiang, Y. B.; Kociok-Kohn, G.; Elmes, R. B. P.; Bull, S. D.; He, X. P.; James, T. D., 'AND'-based fluorescence scaffold for the detection of ROS/RNS and a second analyte. *Chem. Commun.* **2018**, *54* (61), 8466-8469.
41. Cheng, H. Y.; Zou, T.; Xu, Y. L.; Wang, Y.; Wu, A. B.; Dai, J.; Zhang, Y. Z.; Liu, Y., Investigations on the interactions between naphthalimide-based anti-tumor drugs and human serum albumin by spectroscopic and molecular modeling methods. *Luminescence* **2016**, *31* (1), 88-95.
42. Vaya, I.; Lhiaubet-Vallet, V.; Jimenez, M. C.; Miranda, M. A., Photoactive assemblies of organic compounds and biomolecules: drug-protein supramolecular systems. *Chem. Soc. Rev.* **2014**, *43* (12), 4102-4122.
43. Ghuman, J.; Zunszain, P. A.; Petitpas, I.; Bhattacharya, A. A.; Otagiri, M.; Curry, S., Structural basis of the drug-binding specificity of human serum albumin. *J. Mol. Biol.* **2005**, *353* (1), 38-52.
44 Yang, M., Song, Y., Zhang, M., Lin, S., Hao, Z., Liang, Y., Zhang, D., Chen, P. R., *Angew. Chem. Int. Ed*. **2012**, 51, 7674 –7679
45. Asanuma, D.; Sakabe, M.; Kamiya, M.; Yamamoto, K.; Hiratake, J.; Ogawa, M.; Kosaka, N.; Choyke, P. L.; Nagano, T.; Kobayashi, H.; Urano, Y., Sensitive beta-galactosidase-targeting fluorescence probe for visualizing small peritoneal metastatic tumours in vivo. *Nat. Commun.* **2015**, *6*, 6463.
46. Shi, L.; Yan, C.; Ma, Y.; Wang, T.; Guo, Z.; Zhu, W. H., In vivo ratiometric tracking of endogenous β-galactosidase activity using an activatable near-infrared fluorescent probe. *Chem. Commun.* **2019**, *55* (82), 12308-12311.
47. Wang, W.; Vellaisamy, K.; Li, G.; Wu, C.; Ko, C. N.; Leung, C. H.; Ma, D. L., Development of a Long-Lived Luminescence Probe for Visualizing β-Galactosidase in Ovarian Carcinoma Cells. *Anal. Chem.* **2017**, *89* (21), 11679−11684.
48. Meng, A. M.; Wang, Y.; Van Zant, G.; Zhou, D. H., Ionizing radiation and busulfan induce premature senescence in murine bone marrow hematopoietic cells. *Cancer Res.* **2003**, *63* (17), 5414-5419.
49. Cmielova, J.; Havelek, R.; Jiroutova, A.; Kohlerova, R.; Seifrtova, M.; Muthna, D.; Vavrova, J.; Rezacova, M., DNA Damage Caused by Ionizing Radiation in Embryonic Diploid Fibroblasts WI-38 Induces Both Apoptosis and Senescence. *Physiol. Res.* **2011,** *60* (4), 667-677.
50. Childs, B. G.; GLuscevic, M.; Baker, D. J.; Laberge, R. M.; Margquess, D.; Dananberg, J.; van Deursen, J. M., Senescent cells: an emerging target for diseases of aging. *Nat. Rev. Drug Discov.* **2017**, *16* (10), 718-735.
51. Lozano-Torres, B.; Galiana, I.; Rovira, M.; Garrido, E.; Chaib, S.; Bernardos, A.; Munoz-Espin, D.; Serrano, M.; Martinez-Manez, R.; Sancenon, F., An OFF-ON Two-Photon Fluorescent Probe for Tracking Cell Senescence in Vivo. *J. Am. Chem. Soc.* **2017**, *139* (26), 8808-8811.
52. Lee, B. Y.; Han, J. A.; Im, J. S.; Morrone, A.; Johung, K.; Goodwin, E. C.; Kleijer, W. J.; DiMaio, D.; Hwang, E. S., Senescence-associated beta-galactosidase is lysosomal beta-galactosidase. *Aging Cell.* **2006**, *5* (2), 187-195.
53. Kemler, I.; Ennis, M. K.; Neuhauser, C. M.; Dingli, D., In Vivo Imaging of Oncolytic Measles Virus Propagation with Single-Cell Resolution. *Mol. Ther.-Oncolytics* **2019**, *12*, 68-78.
54. Yang, W.; Bai, Y.; Xiong, Y.; Zhang, J.; Chen, S.; Zheng, X.; Meng, X.; Li, L.; Wang, J.; Xu, C.; Yan, C.; Wang, L.; Chang, C. C. Y.; Chang, T-Y.; Zhang, T.; Zhou, P.; Song, B-L.; Liu, W.; Sun, S-C.; Liu, X.; Li, B-L.; Xu, C. Potentiating the antitumour response of CD8+ T cells by modulating cholesterol metabolism. *Nature* **2016**, *531*, 651-655.